

Highly Efficient Photo Rechargeable Supercapacitor based on Ambipolar Interface of Graphitic Carbon Nitride and MXene

Sumana Kumar,*^[a] Anindita Mondal,^[a] Vinod Panwar,^[a] Roopali Shekhawat,^[b] and Abha Misra*^[a]

Dual-functional materials for both the optically and the electrochemically active electrode enable efficient direct storage of solar energy into electrical energy. A photo rechargeable supercapacitor is developed using an ambipolar interface of MXene ($Ti_3C_2T_x$) and protonated graphitic carbon nitride under light illumination. An extraordinarily large increase of 1960% in the electrochemical capacitance is measured under the light illumination (420 nm) compared to its dark capacitance.

Ambipolar interface induces an anomalous increase in the capacitance at an ultra-high scan rate of 1.5×10^5 mV/s under the light illumination. Moreover, the photo-assisted, voltage of ~ 270 mV is generated in the rechargeable supercapacitor. The extraordinary results are attributed to the attractive interface of oppositely charged MXene and protonated graphitic carbon nitride.

Introduction

The demand for energy storage devices with high power density and enhanced energy capacity at high scan rate is increasing day-by-day due to the ever-inflating uses of portable electronic devices.^[1–3] Supercapacitors have become an important class of energy storage devices because of their potential in electric vehicles and consumer electronics. The steep rise in popularity of supercapacitor is attributed to the traits such as longer life cycles, fast charge-discharge capability and high-power density. So far, considerable research has been reported to improve the performance of supercapacitors by developing high-performing electrode materials such as carbon in refined forms,^[4,5] transition metal oxides [$Co(OH)_2$, MnO_2 and CuO]^[6–8] and conducting polymer films^[9] for long life cycles and high power density.^[10] An additional functionality of photo rechargeable energy storage capability in supercapacitors is a novel concept for enabling efficient direct storage of solar energy into electrical energy. Thus, photo rechargeable energy storage is a promising development for the sustainable and eco-friendly use of electrical power for advanced power sources.^[11,12]

Until now, energy storage devices are coupled with the energy conversion systems like solar cells,^[13–15] which involve low level of integration, complexity of circuits, large size,

external wiring, inflexibility, ohmic losses and overall less efficiency. Therefore, to overcome such disadvantages, various functional units should be integrated into a single device.^[16–21] Several modified designs are reported to develop photo rechargeable devices consisting of supercapacitors and solar cells, integrated in a single unit.^[22–24] In one of the reports, an integrated all-inorganic perovskite solar capacitor has been constructed by combining a $CsPbBr_3$ perovskite solar cell and a silica gel supercapacitor unit^[22] for a high operating potential window of 1.2 V, fast rate of photocharging and good stability during charge/discharge cycles. However, the disadvantage of such an architecture is the need for manual switching of electrodes for charging and discharging.

Devices with dual-functional materials, *i.e.*, with both the capabilities of energy conversion and storage will be the way forward to autonomous, self-powered energy storage devices.^[25–28] Optical charging in such devices can be achieved by incorporating a photoactive electrode, which can produce electrical energy from the generation of electron-hole pairs under light illumination. Thus, semiconducting materials that have both photoresponsive properties and capacitive behaviour are reported.^[29–31] However, these devices suffer from lack of spontaneous generation of photovoltage, which predominantly pertains to optimization of the device structure by energy-level alignment.

So far, graphitic materials find a special place in fabrication of highly efficient supercapacitors due to high electrical conductivity, functional surfaces and high surface area. Among these, graphitic carbon nitride (C_3N_4) is an optically active material with a bandgap of 2.75 eV. We developed a photo rechargeable energy storage device using an intimate interfacial contact between oppositely charged semiconducting protonated C_3N_4 (pC_3N_4) and MXene ($Ti_3C_2T_x$). The positively charged surface of pC_3N_4 allows strong mutual electrostatic attraction with MXene (negatively charged

[a] S. Kumar, A. Mondal, V. Panwar, A. Misra

Department of Instrumentation and Applied Physics, Indian Institute of Science, Bangalore, Karnataka 560012, India

E-mail: itiskumarsumana@gmail.com
abha@iisc.ac.in

[b] R. Shekhawat

Center for Nanoscience and Engineering, Indian Institute of Science, Bangalore, Karnataka 560012, India

 Supporting information for this article is available on the WWW under <https://doi.org/10.1002/batt.202300393>

surface).^[32,33] The resulting pC₃N₄/MXene heterointerface is successfully obtained by the π - π stacking and electrostatic attraction. Thus, the resulting nanostructure with high surface area results in much improved and efficient transport of charges across the heterointerfaces. The pC₃N₄ as an electrode material showed self-optical charging capability with a maximum generated voltage of 420 mV_{Ag/AgCl} after exposure to an illumination of 420 nm radiation, which is higher than the voltage obtained without protonated C₃N₄ (300 mV_{Ag/AgCl}). A photo rechargeable pC₃N₄/MXene based solid-state energy storage device demonstrated an areal electrochemical capacitance of 3037.5 μ F/cm² at a scan rate of 1 mV/s and a capacitance enhancement of 1960% is observed under light illumination (420 nm). Moreover, device showed a stable response at an ultra-high scan rate of 150000 mV/s with a significant enhancement in capacitance (214%) under illumination caused by ambipolar transport. Another important attribute of the resulting device is that the light illumination of 420 nm induces a photovoltage of 270 mV without applying any external current or voltage. Thus, photo rechargeable pC₃N₄/MXene based solid-state energy storage device is a novel highly efficient solid-state supercapacitor.

Results and Discussion

Material characterizations

Surface morphologies of both C₃N₄ and pC₃N₄ are shown in scanning electron microscopy (SEM) images (Figure 1a and inset image, respectively). The protonation of C₃N₄ induces exfoliation and reduction in flake size as shown in the inset figure. Figure 1(b) is an SEM image of as-procured MXene. Energy bandgap (E_g) of both the C₃N₄ and pC₃N₄ was measured via UV-vis (ultraviolet-visible) absorption spectra in Figure S1, Figure 1(c) using the tauc approach (inset of Figure S1 and Figure 1(c)) from the Kubelka-Munk relation.^[34,35]

$$\alpha E_{\text{photon}} = K(E_{\text{photon}} - E_g)^{n/2} \quad (1)$$

where, α =absorption coefficient, K =constant, $h\nu=E_{\text{photon}}$, and $n=4$ for C₃N₄. The measured E_g values of C₃N₄ and pC₃N₄ are 2.75 and 2.92 eV (inset), respectively. The observed blue-shift in E_g can be attributed to the π -conjugated system weakening as a consequence of the decreased condensation.^[36]

Photoluminescence (PL) spectra of pristine C₃N₄ and pC₃N₄ in a broad range (440–600 nm) is shown in Figure 1(d) demonstrating emissions from the multiple photoactive energy

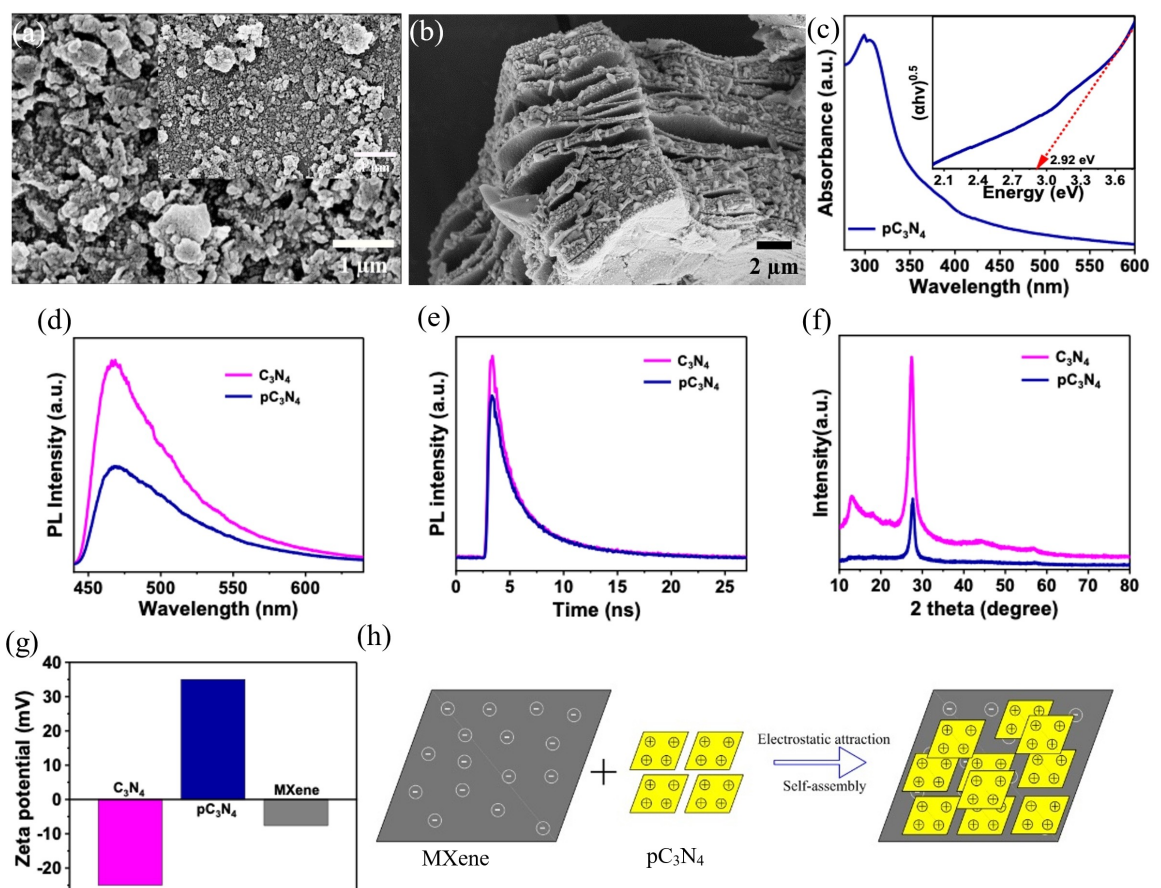


Figure 1. SEM images of a) C₃N₄ and pC₃N₄ (inset). b) SEM image of as-procured MXene. c) UV-vis absorption spectrum and tauc plot (inset) to determine the optical band gap of pC₃N₄. d) PL spectrum and e) time-resolved PL spectrum of C₃N₄ and pC₃N₄ under an excitation by a radiation of wavelength 405 nm. f) XRD patterns of C₃N₄ and pC₃N₄. g) Zeta potentials of C₃N₄, pC₃N₄ and MXene. h) Schematic illustration of electrostatic self-assembling of pC₃N₄ and MXene.

levels of the material. PL intensity of pC_3N_4 is lower compared to C_3N_4 , indicating that the radiative recombination in pC_3N_4 is greatly suppressed. The time-resolved spectra investigated the kinetics of PL decay. The lifetimes of photoexcited charge carriers in C_3N_4 and pC_3N_4 are shown in Figure 1(e). Average lifetimes are obtained using bi-exponential fitting of the PL decay. The calculated average lifetimes for the C_3N_4 and pC_3N_4 are 2.47 ± 0.02 ns and 2.84 ± 0.02 ns, respectively. After protonation, the charge carrier lifetime increased by 15% that indicates an increase in the separation efficiency of photo-generated charge carriers and hence, effectively reduced charge recombination. The decreased PL intensity and extended lifetime are associated with the improved localization of charge on the carbon nitride matrix. The improved localization of charge in protonated C_3N_4 (pC_3N_4) is often observed in various experimental and theoretical studies. Protonation introduces localized positively charged sites ($\text{N}-\text{H}^+$) in heterocycles and the cyano group of the exfoliated C_3N_4 .^[37,38] Further, density functional theory (DFT) calculations have demonstrated the formation of $\text{N}-\text{H}^+$ sites and the alteration of the electronic band structure by Yu. et al and Martin et al.^[39,40] Yang et al. and Du et al. provided X-ray photoelectron spectroscopy (XPS) measurements for evidence of changes in the electronic structure of pC_3N_4 due to protonation.^[37,38] Shifts in binding energies of N and H peaks revealed the formation of $\text{N}-\text{H}^+$ sites. The localized charge carriers at protonation sites act as non-radiative recombination centres. This means that instead of recombining and emitting photons as in PL, charge carriers recombine non-radiatively, leading to a reduction in PL intensity. The effect is consistent with the concept of trap-assisted recombination. Because the trapped charge carriers have a longer lifetime due to their localized nature and hence persist in the material for a longer duration before recombining, resulting in an extended PL lifetime.

The X-ray diffraction (XRD) patterns of C_3N_4 and pC_3N_4 show a hexagonal carbon nitride structure (JCPDS card no. 87-1526) (Figure 1f). The intense peak at 27.38° ($d = 0.325$ nm) of C_3N_4 is a characteristic of interlayer stacking reflection of conjugated aromatic systems, corresponding to the (002) plane for the graphitic materials.^[41] The low angle peak of C_3N_4 is located at 13.1° indexed for (100) plane corresponding to in-plane structure packing of aromatic systems.^[41] The decrease in crystallinity after protonation causes shifting of (002) peak positions to 27.7° with a lower peak intensity. The change in interplanar distance from 0.325 nm to 0.321 nm demonstrates the tighter packing in the aggregates of protonated gC_3N_4 nanosheets. In case of protonated carbon nitride this reduction in interlayer spacing after protonation can be attributed to the electrostatic attraction between the positively charged protons (H^+) introduced during protonation and the negatively charged nitrogen sites in the C_3N_4 structure. The reduction in interlayer spacing after protonation is quite evident and is reported by others as well.^[42,43] Moreover, the Brunauer, Emmett and Teller (BET) surface area of C_3N_4 and pC_3N_4 are $10.4 \text{ m}^2/\text{g}$ and $25.7 \text{ m}^2/\text{g}$, respectively, thus indicating effective exfoliation of C_3N_4 in agreement with the XRD results.^[44]

The $-\text{C}-\text{N}-$ motifs present in C_3N_4 help in an easy protonation using hydrochloric acid. The process of protonation induces surface charge modification from a negatively charged surface to a positively charged surface. Structural modification in C_3N_4 before and after protonation is shown in Figure S2. The measured zeta potential value of pC_3N_4 is $+35$ mV when dispersed in ethanol at pH 7.3 (Figure 1g). The value of zeta potential for C_3N_4 is -25 mV. Therefore, as a marker for successful protonation, zeta potential of C_3N_4 dispersed in ethanol was shifted from -25 to $+35$ mV after protonation. The pC_3N_4 was further modified with the MXene using a self-assembly mechanism operating between pC_3N_4 and MXene due to electrostatic interaction. MXene has a negatively charged surface with a zeta potential value of -7 mV. Hence, self-assembly between negatively charged MXene and positively charged pC_3N_4 was spontaneous as shown by the schematic (Figure 1h). This is driven by electrostatic interactions and $\pi-\pi$ stacking between the two materials. The detailed characterizations of C_3N_4 /MXene and pC_3N_4 /MXene are described in supplementary information, Figures S3–S7.

Electrochemical characterizations

The electrochemical performance of both the C_3N_4 and pC_3N_4 was evaluated in a three-electrode configuration by cyclic voltammetry (CV), galvanostatic charge-discharge (CD) and electrochemical impedance spectroscopy (EIS) measurements. Fluorine-doped tin oxide (FTO) coated glass substrates were used for the working electrode. Figure 2(a) shows CV curves of C_3N_4 and pC_3N_4 at a scan rate of 50 mV/s in the potential (V vs. Ag/AgCl) range of 0–0.8 V using 1 M H_3PO_4 (phosphoric acid) as electrolyte. The CV profile of C_3N_4 depicts a rectangular profile, demonstrating charge storage via the formation of an electric double layer (EDL) at the electrode-electrolyte interface. However, pC_3N_4 shows a slight deviation from the rectangular shape of the CV curve, indicating pseudocapacitive nature. When pC_3N_4 is protonated, some of the nitrogen atoms in the C_3N_4 lattice become protonated, leading to the formation of $\text{N}-\text{H}^+$ bonds to introduce localized positive charge centers in the material. The redox peaks observed in CV curves are associated with the transfer of electrons to or from the protonation sites ($\text{N}-\text{H}^+$ bonds) within the pC_3N_4 structure. These redox reactions involve the protons gaining or losing electrons, leading to changes in their oxidation states. Redox reaction that can occur at protonation sites is the reversible exchange of electrons and protons, which can be represented as: $\text{N}-\text{H}^+ + \text{e}^- \rightleftharpoons \text{N}-\text{H}$. In this reaction, the $\text{N}-\text{H}^+$ site gains an electron to form a neutral $\text{N}-\text{H}$ site. This electron transfer leads to a reduction process (the gain of electrons), which is typically observed as a cathodic peak in the CV curve. Redox reaction can also be attributed to surface functional groups that attached during protonation.^[45] Functional groups like amine groups (NH_2) and other nitrogen-containing moieties can undergo reversible redox reactions by accepting or donating electrons and participating in proton-coupled electron transfer reactions. The charge storage mecha-

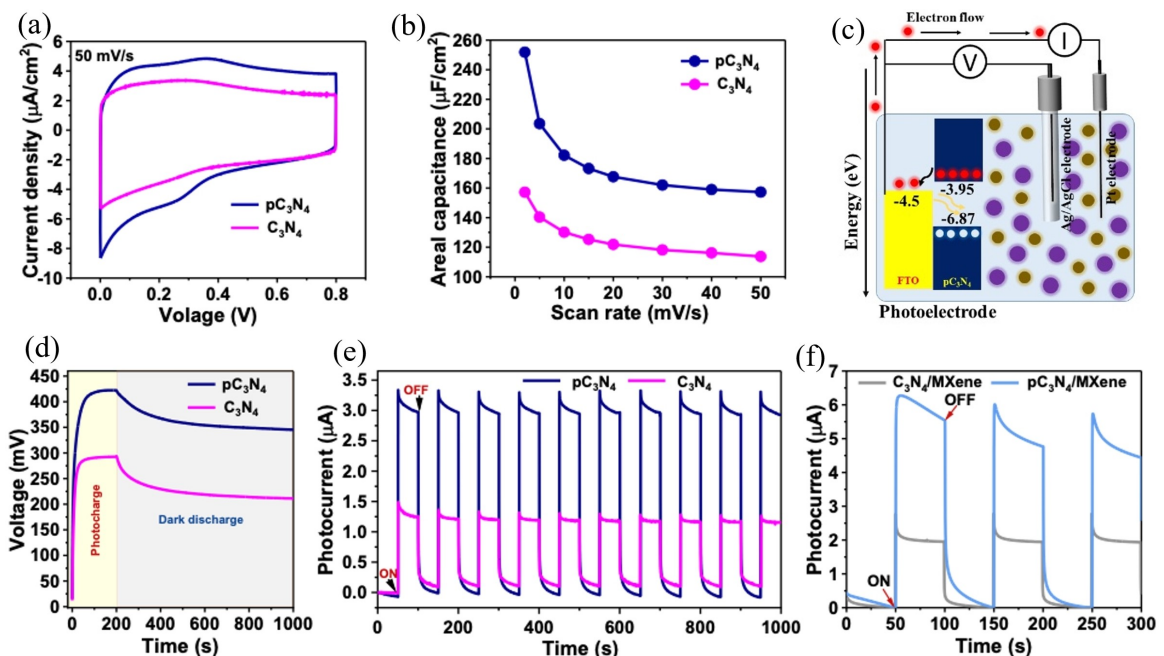


Figure 2. The electrochemical performance of C_3N_4 and pC_3N_4 electrodes in 1 M H_3PO_4 aqueous electrolyte in a three-electrode configuration. a) CV responses at a scan rate of 50 mV/s. b) Areal capacitance of C_3N_4 and pC_3N_4 for a range of scan rates. c) Schematic illustration of photocharging mechanism in a three-electrode configuration of $\text{pC}_3\text{N}_4/\text{FTO}$ electrodes. d) Photo-voltage of pC_3N_4 and C_3N_4 electrodes using light ($\lambda \sim 420$ nm) and discharge in dark condition. e) Cyclic photocurrent of pC_3N_4 and C_3N_4 electrodes at zero bias voltage under dark and illuminated conditions. f) Photocurrent of $\text{C}_3\text{N}_4/\text{MXene}$ and $\text{pC}_3\text{N}_4/\text{MXene}$ electrodes at zero applied voltage under cyclic dark/illuminated conditions.

nism of the electrode was further investigated by Dunn's method for quantitative separation of two components, namely:^[46,47] (more details are provided in the Supporting Information, Figure S8)

- Diffusion independent capacitive contribution from EDL at the electrode-electrolyte interface and/or faradaic charge transfer at the surface-bound atoms (pseudocapacitance).
- Diffusion-controlled faradaic contribution (intercalated pseudocapacitance).

As shown in Figure S8(a and b), the surface capacitive process contributes 85 % and 90 % of the total charge storage at 5 mV/s in the pC_3N_4 and C_3N_4 electrodes, respectively, suggesting a dominated surface capacitive contribution. A higher diffusion-controlled contribution in the pC_3N_4 may be due the presence of terminal groups attached during the protonation and localized positive charge centers.^[45] Figure 2(b) shows the measured areal capacitance with the scan rate. The capacitance of pC_3N_4 is 251, 203, 182, 173, 157 $\mu\text{F}/\text{cm}^2$ at the scan rates of 2, 5, 10, 15 and 50 mV/s, respectively, revealing a maximum of 60% increase in the capacitance at a scan rate of 2 mV/s than that obtained from C_3N_4 based electrode (157, 140, 130, 125, 113 $\mu\text{F}/\text{cm}^2$).

The electrochemical measurements were performed on both the pC_3N_4 and C_3N_4 as photo-electrodes in the presence of light illumination. The photo charging capabilities of the electrodes are obtained under light illumination of wavelength 420 nm in the absence of any external electrical bias and discharging in the dark condition (no illumination) in an

open circuit. Photo charging principle of the working electrode is depicted using the energy level diagrams of the material and FTO, as shown in Figures 2(c) and S9. A maximum photo-voltage in pC_3N_4 is measured 420 mV_{Ag/AgCl} after light illumination for 180 s, which is higher than C_3N_4 (300 mV_{Ag/AgCl}) (Figure 2d). The achieved photo-voltage is lesser than the potential window of galvanostatic charging, which can be attributed to the difference in bias condition for the charging. Light illumination on the electrodes causes a spontaneous photo charging process, whereas galvanostatic charging is obtained upon application of an external current. Moreover, the working electrode is photo charged using light illumination and discharged over a load. The discharging was performed for a total time of 550 s where first it was discharged in the presence of light and later in the dark condition. Once the electrode is continuously exposed to the light, while discharging the output voltage drops to 70% and approaches to a constant value due to the charge balancing between the photo charging and discharging process (Figure S10). After the light is turned off, output voltage of the electrode further drops to 80 mV. During photo charging process, photogenerated electrons in electrode are transported to the counter electrode and the photogenerated accumulated holes attract oppositely charged anions (PO_4^{3-}) in the electrolyte at the electrode to form an EDL. Further, the transfer of electrons in the external circuit or photo charging was confirmed using current time measurement in presence of illumination at zero applied voltage. The result in Figure 2(e) shows that current increases from 0 to 3.2 μA for pC_3N_4 (0 to 1.5 μA for C_3N_4) upon

illumination for 50 s and approaches to 0 μ A in the dark conditions. In addition to a high electrochemical capacitance, pC_3N_4 also exhibits higher photo-electrochemical performance, *i.e.*, generation of higher photocurrent and voltage.

Photocurrents from pC_3N_4 and C_3N_4 composites with MXene were measured using a three-electrode setup, with $\text{C}_3\text{N}_4/\text{MXene}$ and $\text{pC}_3\text{N}_4/\text{MXene}$ as electrodes. These measurements were conducted under light ($\lambda \sim 420$ nm) illumination using 1 M H_3PO_4 electrolyte. As shown in Figure 2(f), the photocurrent intensity for $\text{pC}_3\text{N}_4/\text{MXene}$ is three times higher than that of $\text{C}_3\text{N}_4/\text{MXene}$, indicating efficient charge transfer efficiency at the $\text{pC}_3\text{N}_4/\text{MXene}$ interfaces. The MXene, due to its good electrical conductivity, provides transportation of the photoelectrons generated by the pC_3N_4 , which reduces

the recombination of the photoinduced charge carriers. Therefore, both the SEM and photocurrent responses confirm the formation of advantageous interfacial interaction in the $\text{pC}_3\text{N}_4/\text{MXene}$ composites *via* electrostatic attractive forces.

In view of practical uses of $\text{pC}_3\text{N}_4/\text{MXene}$, the performance of $\text{pC}_3\text{N}_4/\text{MXene}$ was further evaluated in a device configuration, fabricated using a method described experimental section. The photo-electrochemical properties of $\text{pC}_3\text{N}_4/\text{MXene}$ were evaluated using sandwich device configuration of symmetric supercapacitor with $\text{PVA}/\text{H}_3\text{PO}_4$ (poly(vinyl alcohol)/phosphoric acid) electrolyte as shown schematically in Figure 3(a). The energy band diagram of $\text{pC}_3\text{N}_4/\text{MXene}$ with the FTO is shown in the schematic (Figure 3b). CV measurements were conducted to measure photo-assisted changes in the $\text{pC}_3\text{N}_4/\text{MXene}/\text{FTO}$ device at a scan

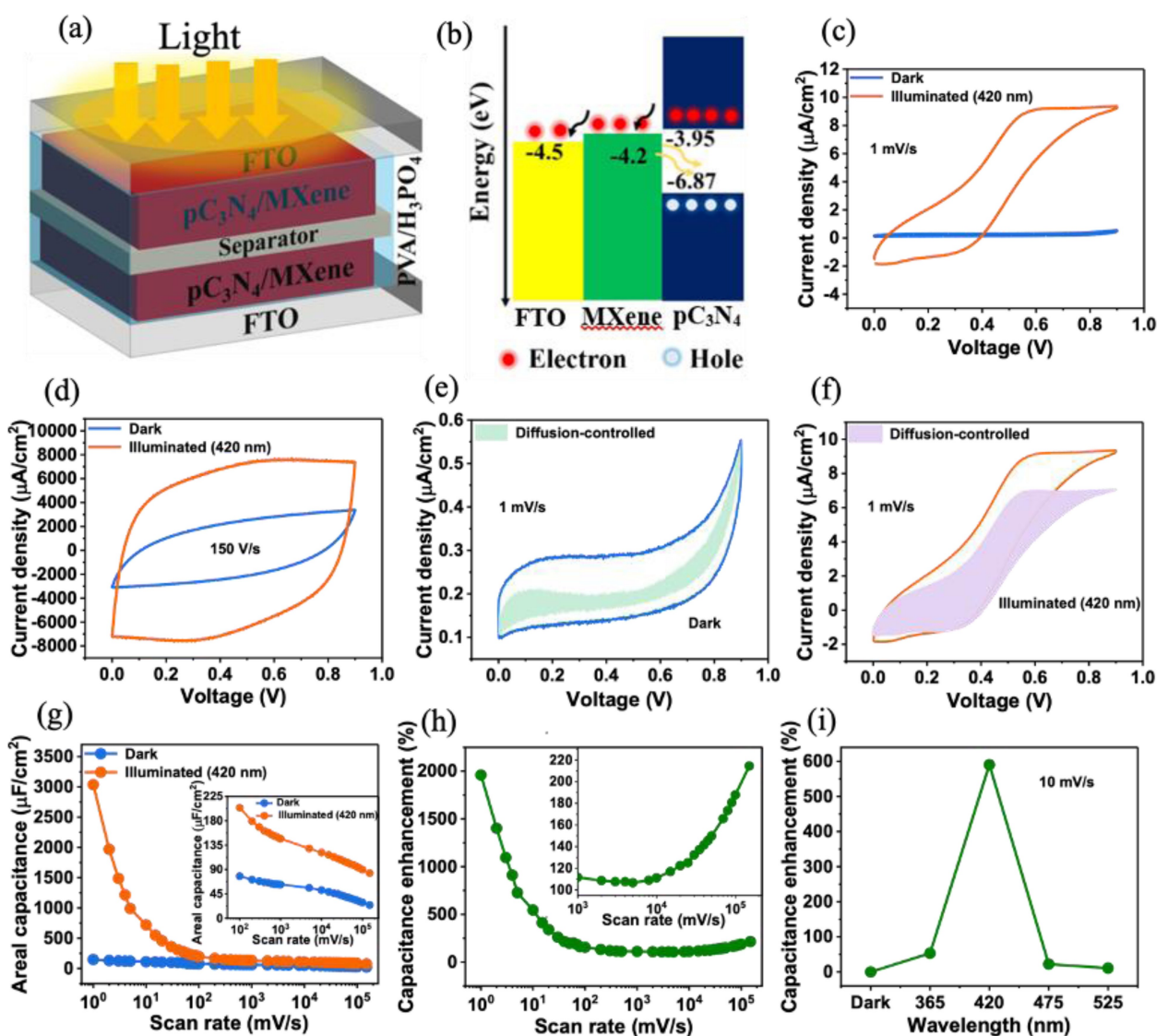


Figure 3. Electrochemical performance of $\text{pC}_3\text{N}_4/\text{MXene}$ device under dark and illuminated conditions. a) Schematic of $\text{pC}_3\text{N}_4/\text{MXene}$ fabricated supercapacitor device. b) Energy band diagram of electrode material with FTO current collector. CV curves in dark and under illumination ($\lambda \sim 420$ nm) at a scan rate of c) 1 mV/s and d) 150 V/s. Quantification of diffusion-controlled contribution to charge storage in e) dark and f) illuminated conditions at 1 mV/s (shaded region). g) Areal capacitance comparison under dark and illuminated conditions (420 nm) for a range of scan rates; Inset: Areal capacitance comparison at high scan rates. h) Capacitance enhancement under illumination (420 nm) compared to dark condition for a range of scan rates. Inset: Capacitance enhancement at high scan rates. i) Capacitance enhancement under illumination with the variation in light wavelength.

rate from 1 to 150000 mV/s under both dark and illuminated conditions ($\lambda \sim 420$ nm) (Figure S11 and S12). The $\text{pC}_3\text{N}_4/\text{MXene}$ device in dark condition presents nearly rectangular CV response up to a maximum scan rate of 1 V/s, which is a typical of EDL capacitor. At higher scan rates of 50–150 V/s, the CV responses slightly deviate from rectangular shape indicating the presence of resistive behaviour. Thus, the device capability of providing nearly rectangular CV response up to ultra-high scan rate indicates high-power handling capabilities. In presence of light illumination, the device exhibits a surge in the current as well as possess larger area of the CV curve at all the scan rates compared to the dark condition (Figures 3c and d, S13).

Figure 3(c and d) exhibits the enhanced CV responses under radiation illumination condition ($\lambda \sim 420$ nm) at a scan rate of 1 mV/s and 150 V/s, respectively. The illumination induced CV curves at lower scan rates up to 1 V/s show non-rectangular shape and at higher scan rates the CV curves show again a rectangular shape. The occurrence of redox peaks at low scan rates in the cyclic voltammetry (CV) curves of the $\text{pC}_3\text{N}_4/\text{MXene}$ composite electrode under illumination suggests that the redox reactions between the electrode materials and electrolyte ions primarily occur under light illumination. This behavior indicates that light plays a significant role in triggering electrochemical processes in the composite electrode. Under illumination photons from the light source are absorbed by the pC_3N_4 component of the composite electrode, creating electron-hole pairs (e^- and h^+). Electrons (e^-) are transferred to the MXene component due to its excellent electron conductivity, while the holes (h^+) remain in the pC_3N_4 . Electrons (e^-) generated by the photo-excitation process can participate in cathodic reactions at the electrode surface, leading to reduction reactions. Holes (h^+) generated during photoexcitation can participate in anodic reactions, leading to oxidation reactions. Moreover, the $\text{pC}_3\text{N}_4/\text{MXene}$ device is capable of providing significant photo-electrochemical charge storage for an ultra-long range of scan rates from 1 to 150000 mV/s. Again, Dunn's method^[46,47] is used for understanding the charge storage mechanism in $\text{pC}_3\text{N}_4/\text{MXene}$ device in both the dark and illuminated conditions. Figure 3(e and f) shows diffusion-controlled contribution of the device in a shaded area at 1 mV/s scan rate in dark and illumination conditions, respectively. Figure S14 exhibits contribution ratios for a range of scan rates. At very low scan rates (1 to 5 mV/s), significant surface capacitive-controlled capacitance is obtained in dark condition, whereas under illumination at lower scan rate, the diffusion-controlled capacitance predominantly increases as presented in Figure S14. However, at higher scan rate, the device shows a dominated surface capacitive response in both dark and illuminated conditions (Figure S15a–d). Figure S15(a and b) shows diffusive contribution of the device by the shaded area at a scan rate of 500 mV/s in dark and illuminated conditions, respectively. Figure S15(c and d) shows the contribution ratios for a range of high scan rates in dark and illuminated conditions, respectively. The calculated areal capacitance of $\text{pC}_3\text{N}_4/\text{MXene}$ device in the

dark and illuminated conditions for a range of scan rates (1–150000 mV/s) is shown in Figure 3(g). A significant enhancement in electrochemical capacitance is observed in the presence of light illumination. The $\text{pC}_3\text{N}_4/\text{MXene}$ device in dark condition exhibited an areal capacitance of about $147.5 \mu\text{F}/\text{cm}^2$ at a scan rate of 1 mV/s, which is dropped to $94.9 \mu\text{F}/\text{cm}^2$, $77.7 \mu\text{F}/\text{cm}^2$, $65.5 \mu\text{F}/\text{cm}^2$, $62.3 \mu\text{F}/\text{cm}^2$ at a scan rate of 50 mV/s, 100 mV/s, 500 mV/ and 1000 mV/s, respectively, which is about 64.3%, 52.6%, 44.4% and 42.3%, respectively higher of its initial capacitance at a scan rate of 1 mV/s. Moreover, capacitance was further reduced to $46.2 \mu\text{F}/\text{cm}^2$, $36.96 \mu\text{F}/\text{cm}^2$, $29.03 \mu\text{F}/\text{cm}^2$ and $24.35 \mu\text{F}/\text{cm}^2$ at an ultra-high scan rate of 20000, 50000, 100000, and 150000 mV/s, respectively (Figure 3g). The areal capacitance value at a scan rate of 150000 is about 16.5% of the initial capacitance recorded at a 1 mV/s scan rate. The $\text{pC}_3\text{N}_4/\text{MXene}$ device under illumination (420 nm) exhibits areal capacitance of $3037.5 \mu\text{F}/\text{cm}^2$ at a scan rate of 1 mV/s, which dropped to $281.9 \mu\text{F}/\text{cm}^2$, $198 \mu\text{F}/\text{cm}^2$, $139 \mu\text{F}/\text{cm}^2$, $131.8 \mu\text{F}/\text{cm}^2$ at a scan rate of 50 mV/s, 100 mV/s, 500 mV/ and 1000 mV/s, respectively. Moreover, the device shows areal capacitance of $102.8 \mu\text{F}/\text{cm}^2$, $92.4 \mu\text{F}/\text{cm}^2$, $83.59 \mu\text{F}/\text{cm}^2$ and $76.6 \mu\text{F}/\text{cm}^2$ under illumination at an ultra-high scan rate of 20000, 50000, 100000, and 150000 mV/s, respectively (Figure 3g). Figure 3(h) exhibits significant enhancement in capacitance under illumination of visible light for a wide range of scan rates (1 mV/s–150 V/s). Upon illumination, an anomalously high areal capacitance of 1960% is observed under 420 nm light illumination compared to dark condition (Figure 3h). Interestingly, the device under illumination showed a decreasing trend in percentage enhancement in capacitance up to 1000 mV/s and then increased, as shown in inset of Figure 3(h). A decrease in percentage enhancement in capacitance is due to the insufficient time for charge interaction causing lesser charges to be stored in the system. Moreover, an increase in percentage enhancement in capacitance could be attributed to the light enhanced ambipolar transport at higher scan rates.^[48] At higher scan rate light illumination lead to the development of space charge due to the reduced activation energy of ions for the migration as was observed earlier by Zhao et al.^[49] More accumulation of ions in EDL under light illumination increases EDL capacitance. The device was also tested in the presence of other wavelengths, e.g., 365 nm, 475 nm, 525 nm to evaluate optical charging capabilities, as shown in Figure 3(i). The obtained results suggested a negligible increase in the photo-assisted changes in the electrochemical capacitance for other wavelengths compared to 420 nm which can be attributed to the near band-gap energy of 2.95 eV for the pC_3N_4 (~ 2.92 eV). Furthermore, the $\text{pC}_3\text{N}_4/\text{MXene}$ device capacitance response is observed with different intensity of light (420 nm). The photo-assisted electrochemical capacitance enhanced from ~100% to 200% with increasing light intensity from ~5 to 20 mW/cm² (Figure S16).

The electrochemical performance of $\text{pC}_3\text{N}_4/\text{MXene}$ device under illumination was evaluated using CD measurements for a range of current densities. The CD curves of the device in dark

conditions show a triangular shape at a current density of $1.25 \mu\text{A}/\text{cm}^2$, indicating dominating EDL capacitance behaviour, well-matched with the observation from the CV curves (Figure S17). Under illumination, the device exhibits larger charge-discharge time along with non-linear CD responses due to the presence of pseudocapacitive charge storage along with EDL (Figure S17). The calculated areal capacitances from the CD curves exhibit higher performance in presence of illumination compared to dark at all current densities, as shown in Figure S18. Under illumination, the devices recorded a maximum areal capacitance of $500 \mu\text{F}/\text{cm}^2$ at a current density of $10 \mu\text{A}/\text{cm}^2$. The photo-electrochemical change is verified from CV and CD results in pC₃N₄/MXene solid-state device. The advantage of pC₃N₄ compared to C₃N₄ was discussed earlier using electrochemical and photocurrent measurements in three-electrode setup. Moreover, the advantage of adding MXene as electrode material further understood by comparing pC₃N₄/MXene with the electrochemical response of pC₃N₄ device. CV measurements in pC₃N₄ device were performed in dark and under illumination using different wavelengths of light. The measured areal capacitances obtained from CV curve in dark and under illumination were compared and shown in Figure S19(a). The pC₃N₄ device shows a maximum capacitance value of $210 \mu\text{F}/\text{cm}^2$ at a scan rate of 10 mV/s under light illumination of 420 nm and $110 \mu\text{F}/\text{cm}^2$ at the same scan rate in dark conditions. The calculated capacitance enhancement under illumination of different wavelengths of light, when compared to dark condition, is shown in Figure S19(b). The maximum

capacitance enhancement of $\sim 90\%$ obtained under illumination of 420 nm light is much lesser than the capacitance enhancement obtained in the pC₃N₄/MXene device ($\sim 600\%$).

Apart from photo-assisted enhancement in the electrochemical capacitance, the pC₃N₄/MXene device can be charged in the presence of light without any external electrical bias. Figure 4(a) shows the optical charging of the device with the generated voltage of $\sim 270 \text{ mV}$ when illuminated for 250 s and subsequent discharge in the dark for a prolonged time. Under illumination, the photoexcited electrons travel from the photoelectrode to the counter electrode *via* the external circuit, causing adsorption of cations (H^+) at the electrode-electrolyte interface to form a double-layer at the interface. While the photogenerated holes attract anions towards the photoelectrode for adsorption at the electrode-electrolyte interface. The obtained photovoltage in pC₃N₄/MXene device due to light exposure is compared with previously reported supercapacitors utilized with photo-assisted measurements (Table S1). The entire process results in optical charging of the device under light exposure. The stability of the device is investigated using repeated optical charging and discharging in dark condition for each cycle of 100 s , shown in Figure S20. The charging of pC₃N₄/MXene under illumination can be further confirmed from the chronoamperometry measurement (i.e., current versus time) measurement in absence of externally applied voltage. Chronoamperometry measurements were performed using different wavelengths of light, e.g., 525 , 475 , 365 , and 420 nm as shown in Figure 4(b). The measured photocurrent under the

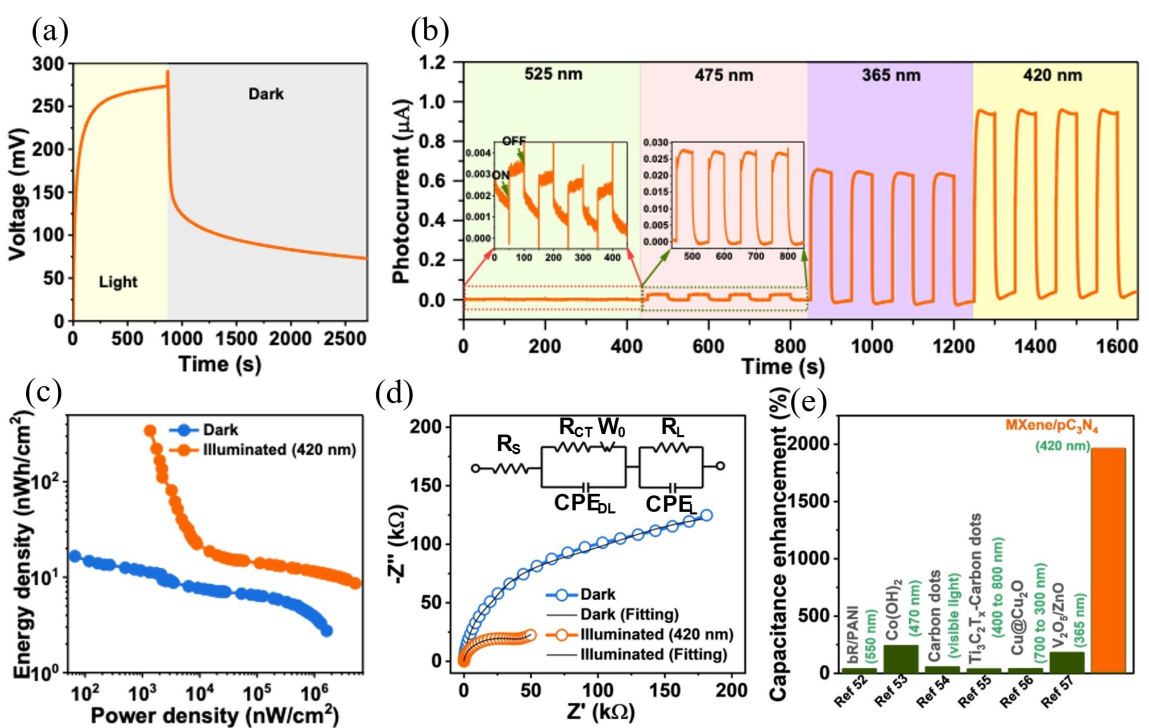


Figure 4. a) Photocharge of pC₃N₄/MXene device using 420 nm light and discharge in dark conditions in absence of external bias condition. b) Photocurrent of pC₃N₄/MXene device under cyclic dark and illuminated conditions with different wavelength of light at zero applied voltage. c) Ragone plot of pC₃N₄/MXene device in dark and illuminated conditions. d) Nyquist plot of pC₃N₄/MXene device in dark and illuminated conditions, Randle's equivalent circuit model depicted in the inset. e) Capacitance enhancement comparison of our pC₃N₄/MXene device with previously reported photo charge-assisted devices.

illumination of 420 nm is substantially higher than other wavelengths as shown in Figure 4(b), which is attributed to near higher energy of 420 nm (~2.95 eV) light to the band-gap of pC_3N_4 (~2.92 eV). Furthermore, the advantage of $\text{pC}_3\text{N}_4/\text{MXene}$ compared to pC_3N_4 device is understood using photocurrent measurement at $V=0$ condition. The measured photocurrent for pC_3N_4 device is much lower than $\text{pC}_3\text{N}_4/\text{MXene}$ device (Figure S21), indicating a meaningful introduction of MXene for highly photoactive electrode materials.

The areal energy density and power density of $\text{pC}_3\text{N}_4/\text{MXene}$ device in dark and illumination conditions are shown in Figure 4(c). Our $\text{pC}_3\text{N}_4/\text{MXene}$ device demonstrated maximum areal energy density of 341.7 nWh/cm² at a power density of 1366.8 nW/cm² under illumination, which is higher than the values obtained for dark condition (16.58 nWh/cm² at 66.34 nW/cm²). A 20-fold increase in energy density is obtained for the device under 420 nm light illumination than dark condition. Furthermore, $\text{pC}_3\text{N}_4/\text{MXene}$ device in illuminated and dark conditions exhibit maximum power density of 5170 $\mu\text{W}/\text{cm}^2$ and 1643 $\mu\text{W}/\text{cm}^2$, respectively.

EIS was used for understanding ion transport properties of the $\text{pC}_3\text{N}_4/\text{MXene}$ device in dark and illuminated condition for a range of frequencies (0.01 Hz to 100 kHz). The Nyquist plot for the device in the two conditions is shown in Figure 4(d). The inset in Figure 4(d) illustrates the equivalent circuit employed to fit the EIS data in this study. The results of the fitting for the various circuit elements can be found in Table S2. The term " R_s " is referred as solution resistance, corresponds to the equivalent series resistance. This component typically characterizes the resistance associated with the electrolyte, in conjunction with the internal resistance of the electrode.^[50] In this study, the R_s value was determined to be 15.18 Ω under dark condition and 14.73 Ω under illuminated condition. A slight reduction in R_s suggests a minor decrease in the solution resistance under illumination, indicating a subtle enhancement in ionic conductivity.^[43] The " R_{CT} " as the charge transfer resistance, signifies the rate at which redox reactions occur at the electrode-electrolyte interface.^[51] A substantial reduction in R_{CT} following illumination is indicative of improved charge transfer kinetics. The " CPE_{DL} " is a constant phase element (CPE) that represents the double layer capacitance. This capacitance arises at interfaces between solids and ionic solutions due to the separation of ionic and/or electronic charges.^[50] The " W_0 " represents the Warburg element, reflecting the diffusion of ions into the electrode, particularly in the intermediate frequency range. This element accounts for the frequency-dependent nature of the diffusion process. The " R_{L} " denotes the leakage resistance, which is usually very high and can often be disregarded in the circuit analysis.^[51] CPE_{L} is used to describe pseudocapacitance, which arises due to voltage-dependent Faradaic charge transfer processes.^[50]

The capacitance enhancement in $\text{pC}_3\text{N}_4/\text{MXene}$ device due to light exposure is compared with previously reported supercapacitors utilized with photo-assisted enhancement e.g., bR/PANI supercapacitor (550 nm, 37.2%),^[52] Co(OH)₂ supercapacitor (470 nm, 240%),^[53] carbon dot supercapacitor (visible light, 54.4%),^[54] Ti₃C₂T_x-carbon dots supercapacitors (400 to 800 nm,

35.9%),^[55] nanoporous Cu@Cu₂O supercapacitor (700 to 300 nm, 37.9%),^[56] V₂O₅/ZnO^[57] (365 nm, 178%) (Figure 4e). We report the considerably high enhancement of capacitance (~1960%) under illumination among the state-of-the art reported energy storage devices for photo charged enhanced capacitance.

Conclusion

Charging of supercapacitors rely on external power sources. This work demonstrates a photo rechargeable supercapacitor using a highly photoactive heterojunction of $\text{pC}_3\text{N}_4/\text{MXene}$ via an electrostatic self-assembly approach for simultaneous storing of energy and charging by light. Photo electrode of pC_3N_4 provided higher electrochemical activity (60% enhancement in capacitance), enhancement in photocurrent (113% increase), high photovoltage (420 mV, 40% increase) than bulk C₃N₄. The intimate contact between positively charged pC_3N_4 and negatively charged MXene sheets provided accelerated photo-induced electrons transfer from the conduction band of pC_3N_4 to the metallic MXene. These reflect in areal capacitance under illumination than dark conditions and photocurrent measurement in the $\text{pC}_3\text{N}_4/\text{MXene}$ device with an enhancement of ~567% and ~480% than pure pC_3N_4 device. The photo-rechargeable supercapacitor achieved a capacitance enhancement of 1960% under illumination of 420 nm light than dark conditions and a photo voltage of 270 mV.

Experimental Section

Synthesis of graphitic C₃N₄ and protonation of C₃N₄

In a typical synthesis procedure, 5 g of melamine (C₃H₆N₆) was transferred into a ceramic crucible with 80% volume filling and covered by a lid. The crucible was placed in a muffle furnace to heat at 550 °C for 4 h under ambient air environment, thereafter, the furnace was cooled down to room temperature. The yellow colour solid of C₃N₄ was collected and milled into powder for the protonation. The protonation treatment was commenced by stirring of as-obtained C₃N₄ (3 g) with hydrochloric acid (37%, 30 mL) for 3 h at 80 °C and using repetitive centrifugal washing with the de-ionized (DI) water until the neutral solution was obtained.^[45] The product was dried at 100 °C for overnight. The resulting powder was dispersed in 30 mL ethanol and sonicated for 2 h. Furthermore, pC_3N_4 was obtained through vacuum filtration of the suspension and drying at 100 °C overnight.

Preparation of photo-electrode and supercapacitor device

Photo-electrodes for the three-electrode measurements were prepared on FTO coated glass substrate as the working electrode. As-prepared materials (C₃N₄ and pC_3N_4) (90 wt %) were dispersed in ethanol solvent (10 mL) and sonicated for 2 h. Further, polyvinylidene fluoride (PVDF) of 10 wt % was added to the dispersion and stirred for 6 h. The homogeneous solution was spray coated using argon as the carrier gas onto the FTO coated glass substrate at 120 °C. Area of the electrode material deposited on the substrate was ~1×1.5 cm² with a mass loading of ~2.5 mg/cm².

The device fabrication commenced with dispersing 90 wt% of pC_3N_4 and 10 wt% MXene (procured from nanochemazone) together in ethanol solvent (10 ml) and sonicated for 4 h. The homogeneous solution was spray coated using argon as a carrier gas onto the FTO coated glass substrate at 120 °C. A copper strip was attached on the uncoated FTO with silver paste enabling strong electrical contact. The device is assembled using two pieces of material-coated FTO electrodes separated by PVA/ H_3PO_4 (poly(vinyl alcohol)/phosphoric acid) gel coated filter paper. The gel electrolyte, PVA/ H_3PO_4 , was prepared by mixing 6 g PVA and 6 g H_3PO_4 in 60 mL DI water, followed by vigorous stirring for 2 h at 85 °C. Finally, pC_3N_4 /MXene/FTO device was kept in a laminar hood overnight to remove excess water present in the electrolyte. Similarly, a device without MXene (pC_3N_4 /FTO) was also prepared using the same procedures as described above.

Electrochemical characterizations

CV, CD and EIS were carried out in two- and three-electrode configurations using the CHI660E electrochemical workstation at room temperature. Three-electrode measurements were carried out using standard three-electrode cell where material coated FTO electrodes was used as working electrode, Ag/AgCl as reference electrodes and platinum (Pt) wire as a counter electrode. An aqueous solution of 1 M H_3PO_4 was used as the electrolyte. EIS was measured using an input ac signal of 5 mV in the frequency range from 0.01 Hz to 100 kHz. Photo-assisted measurements were performed under light illumination using light emitting diodes of wavelengths 365, 420, 475, and 525 nm.

Acknowledgements

A.M. would like to acknowledge funding from SERB power fellowship (SPR/2020/000103) and funding from MoE-STAR (STARS2/2023-0589). S.K. acknowledges PS Chauhan for the experimental discussion.

Conflict of Interests

The authors declare no conflict of interest.

Data Availability Statement

The data that support the findings of this study are available from the corresponding author upon reasonable request.

Keywords: photo rechargeable supercapacitor · carbon nitride · MXene · self-powered

- [1] C. Schütter, S. Pohlmann, A. Balducci, *Adv. Energy Mater.* **2019**, *9*, 1–11.
- [2] L. Dong, C. Xu, Y. Li, Z. H. Huang, F. Kang, Q. H. Yang, X. Zhao, *J. Mater. Chem. A Mater.* **2016**, *4*, 4659–4685.
- [3] F. Zhao, W. Liu, T. Qiu, W. Bin Gong, W. Ma, Q. Li, F. Li, F. Geng, *ACS Nano* **2020**, *14*, 603–610.
- [4] J. Lin, C. Zhang, Z. Yan, Y. Zhu, Z. Peng, R. H. Hauge, D. Natelson, J. M. Tour, *Nano Lett.* **2013**, *13*, 72–78.
- [5] J. Li, S. Sollami Delektta, P. Zhang, S. Yang, M. R. Lohe, X. Zhuang, X. Feng, M. Östling, *ACS Nano* **2017**, *11*, 8249–8256.
- [6] H. Sheng, X. Zhang, Y. Ma, P. Wang, J. Zhou, Q. Su, W. Lan, E. Xie, C. J. Zhang, *ACS Appl. Mater. Interfaces* **2019**, *11*, 8992–9001.
- [7] S. E. Moosavifard, M. F. El-Kady, M. S. Rahmanifar, R. B. Kaner, M. F. Mousavi, *ACS Appl. Mater. Interfaces* **2015**, *7*, 4851–4860.
- [8] L. Zhang, P. Zhu, F. Zhou, W. Zeng, H. Su, G. Li, J. Gao, R. Sun, C. P. Wong, *ACS Nano* **2016**, *10*, 1273–1282.
- [9] M. Yoonessi, A. Borenstein, M. F. El-Kady, C. L. Turner, H. Wang, A. Z. Stieg, L. Pilon, *ACS Appl. Energ. Mater.* **2019**, *2*, 4629–4639.
- [10] K. C. Ho, L. Y. Lin, *J. Mater. Chem. A Mater.* **2019**, *7*, 3516–3530.
- [11] A. Gurung, Q. Qiao, *Joule* **2018**, *2*, 1217–1230.
- [12] Q. Zeng, Y. Lai, L. Jiang, F. Liu, X. Hao, L. Wang, M. A. Green, *Adv. Energy Mater.* **2020**, *10*, 1–30.
- [13] S. Liao, X. Zong, B. Seger, T. Pedersen, T. Yao, C. Ding, J. Shi, J. Chen, C. Li, *Nat. Commun.* **2016**, *7*, DOI 10.1038/ncomms11474.
- [14] D. Schmidt, M. D. Hager, U. S. Schubert, *Adv. Energy Mater.* **2016**, *6*, 1–11.
- [15] Y. Hu, Y. Bai, B. Luo, S. Wang, H. Hu, P. Chen, M. Lyu, J. Shapter, A. Rowan, L. Wang, *Adv. Energy Mater.* **2019**, *9*, 1–9.
- [16] H. D. Um, K. H. Choi, I. Hwang, S. H. Kim, K. Seo, S. Y. Lee, *Energy Environ. Sci.* **2017**, *10*, 931–940.
- [17] P. Chen, G. R. Li, T. T. Li, X. P. Gao, *Adv. Sci.* **2019**, *6*, 1–8.
- [18] W. Guo, X. Xue, S. Wang, C. Lin, Z. L. Wang, *Nano Lett.* **2012**, *12*, 2520–2523.
- [19] J. Liang, G. Zhu, C. Wang, P. Zhao, Y. Wang, Y. Hu, L. Ma, Z. Tie, J. Liu, Z. Jin, *Nano Energy* **2018**, *52*, 239–245.
- [20] J. Liang, G. Zhu, Z. Lu, P. Zhao, C. Wang, Y. Ma, Z. Xu, Y. Wang, Y. Hu, L. Ma, T. Chen, Z. Tie, J. Liu, Z. Jin, *J. Mater. Chem. A Mater.* **2018**, *6*, 2047–2052.
- [21] L. Qin, J. Jiang, Q. Tao, C. Wang, I. Persson, M. Fahlman, P. O. A. Persson, L. Hou, J. Rosen, F. Zhang, *J. Mater. Chem. A Mater.* **2020**, *8*, 5467–5475.
- [22] J. Liang, G. Zhu, C. Wang, P. Zhao, Y. Wang, Y. Hu, L. Ma, Z. Tie, J. Liu, Z. Jin, *Nano Energy* **2018**, *52*, 239–245.
- [23] J. Liang, G. Zhu, Z. Lu, P. Zhao, C. Wang, Y. Ma, Z. Xu, Y. Wang, Y. Hu, L. Ma, T. Chen, Z. Tie, J. Liu, Z. Jin, *J. Mater. Chem. A Mater.* **2018**, *6*, 2047–2052.
- [24] L. Qin, J. Jiang, Q. Tao, C. Wang, I. Persson, M. Fahlman, P. O. A. Persson, L. Hou, J. Rosen, F. Zhang, *J. Mater. Chem. A Mater.* **2020**, *8*, 5467–5475.
- [25] Y. Zhou, S. Zhang, Y. Ding, L. Zhang, C. Zhang, X. Zhang, Y. Zhao, G. Yu, *Adv. Mater.* **2018**, *30*, 1–7.
- [26] Y. Ding, X. Guo, K. Ramirez-Meyers, Y. Zhou, L. Zhang, F. Zhao, G. Yu, *Energy Environ. Sci.* **2019**, *12*, 3370–3379.
- [27] Q. Li, Y. Liu, S. Guo, H. Zhou, *Nano Today* **2017**, *16*, 46–60.
- [28] L. Bai, H. Huang, S. Zhang, L. Hao, Z. Zhang, H. Li, L. Sun, L. Guo, H. Huang, Y. Zhang, *Adv. Sci.* **2020**, *7*, 1–9.
- [29] C. An, Z. Wang, W. Xi, K. Wang, X. Liu, Y. Ding, *J. Mater. Chem. A Mater.* **2019**, *7*, 15691–15697.
- [30] H. Li, M. Wang, G. Qi, Y. Xia, C. Li, P. Wang, M. Sheves, Y. Jin, *J. Mater. Chem. A Mater.* **2020**, *8*, 8268–8272.
- [31] S. K. Ravi, P. Rawding, A. M. Elshahawy, K. Huang, W. Sun, F. Zhao, J. Wang, M. R. Jones, S. C. Tan, *Nat. Commun.* **2019**, *10*, 1–10.
- [32] Y. Zhang, A. Thomas, M. Antonietti, X. Wang, *J. Am. Chem. Soc.* **2009**, *131*, 50–51.
- [33] J. Kang, S. Byun, S. Kim, J. Lee, M. Jung, H. Hwang, T. W. Kim, S. H. Song, D. Lee, *ACS Appl. Energ. Mater.* **2020**, *3*, 9226–9233.
- [34] Q. Guo, Y. Zhang, H. S. Zhang, Y. Liu, Y. J. Zhao, J. Qiu, G. Dong, *Adv. Funct. Mater.* **2017**, *27*, 1–12.
- [35] A. Chen, R. Liu, X. Peng, Q. Chen, J. Wu, *ACS Appl. Mater. Interfaces* **2017**, *9*, 37191–37200.
- [36] D. J. Martin, K. Qiu, S. A. Shevlin, A. D. Handoko, X. Chen, Z. Guo, J. Tang, *Angew. Chem. Int. Ed.* **2014**, *53*, 9240–9245.
- [37] S. Yang, Y. Gong, J. Zhang, L. Zhan, L. Ma, Z. Fang, R. Vajtai, X. Wang, P. M. Ajayan, *Adv. Mater.* **2013**, *25*, 2452–2456.
- [38] X. Du, G. Zou, Z. Wang, X. Wang, *Nanoscale* **2015**, *7*, 8701–8706.
- [39] S. Yu, J. Li, Y. Zhang, M. Li, F. Dong, T. Zhang, H. Huang, *Nano Energy* **2018**, *50*, 383–392.
- [40] D. J. Martin, K. Qiu, S. A. Shevlin, A. D. Handoko, X. Chen, Z. Guo, J. Tang, *Angew. Chem. Int. Ed.* **2014**, *53*, 9240–9245.
- [41] Q. Guo, Y. Zhang, H. S. Zhang, Y. Liu, Y. J. Zhao, J. Qiu, G. Dong, *Adv. Funct. Mater.* **2017**, *27*, 1–12.
- [42] B. Liu, L. Ye, R. Wang, J. Yang, Y. Zhang, R. Guan, L. Tian, X. Chen, *ACS Appl. Mater. Interfaces* **2018**, *10*, 4001–4009.
- [43] Y. Zhang, A. Thomas, M. Antonietti, X. Wang, *J. Am. Chem. Soc.* **2009**, *131*, 50–51.
- [44] S. Yang, Y. Gong, J. Zhang, L. Zhan, L. Ma, Z. Fang, R. Vajtai, X. Wang, P. M. Ajayan, *Adv. Mater.* **2013**, *25*, 2452–2456.

- [45] C. Ye, J. X. Li, Z. J. Li, X. B. Li, X. B. Fan, L. P. Zhang, B. Chen, C. H. Tung, L. Z. Wu, *ACS Catal.* **2015**, *5*, 6973–6979.
- [46] J. Wang, J. Polleux, J. Lim, B. Dunn, *J. Phys. Chem. C* **2007**, *111*, 14925–14931.
- [47] T. Brezesinski, J. Wang, S. H. Tolbert, B. Dunn, *Nat. Mater.* **2010**, *9*, 146–151.
- [48] R. A. Kerner, B. P. Rand, *J. Phys. Chem. Lett.* **2018**, *9*, 132–137.
- [49] Y. C. Zhao, W. K. Zhou, X. Zhou, K. H. Liu, D. P. Yu, Q. Zhao, *Light-Sci. Appl.* **2017**, *6*, e16243–8.
- [50] B. E. Conway, V. Birss, J. Wojtowicz, *J. Power Sources* **1997**, *66*, 1–14.
- [51] W. Wang, S. Guo, I. Lee, K. Ahmed, J. Zhong, Z. Favors, F. Zaera, M. Ozkan, C. S. Ozkan, *Sci. Rep.* **2014**, *4*, 1–9.
- [52] H. Li, M. Wang, G. Qi, Y. Xia, C. Li, P. Wang, M. Sheves, Y. Jin, *J. Mater. Chem. A Mater.* **2020**, *8*, 8268–8272.
- [53] S. Kalasina, P. Pattanasattayavong, M. Suksomboon, N. Phattharasupakun, J. Wuttiprom, M. Sawangphruk, *Chem. Commun.* **2017**, *53*, 709–712.
- [54] H. Wang, J. Cao, Y. Zhou, Z. Wang, Y. Zhao, Y. Liu, H. Huang, M. Shao, Y. Liu, Z. Kang, *Nanoscale* **2020**, *12*, 17925–17930.
- [55] H. Wang, J. Cao, Y. Zhou, X. Wang, H. Huang, Y. Liu, M. Shao, *Nano Res.* **2021**, *14*, 3886–3892.
- [56] C. An, Z. Wang, W. Xi, K. Wang, X. Liu, Y. Ding, *J. Mater. Chem. A Mater.* **2019**, *7*, 15691–15697.
- [57] P. S. Chauhan, S. Kumar, A. Mondal, P. Sharma, M. N. Parekh, V. Panwar, A. M. Rao, A. Misra, *J. Mater. Chem. A Mater.* **2022**, *11*, 95–107.

Manuscript received: September 15, 2023

Revised manuscript received: October 30, 2023

Accepted manuscript online: October 30, 2023

Version of record online: November 20, 2023